Gravitational effect on the cell in bio-fluid suspension

Anirudh Murali [1, 2] and Ram Rup Sarkar [1, 2*]

[1] Chemical Engineering and Process Development, CSIR - National Chemical Laboratory, Pune, India

[2] Academy of Scientific and Innovative Research (AcSIR), Ghaziabad 201002, India

[*] Corresponding author. Tel: +91-20-2590 3040; +91-20-2590 2161;
Email: rr.sarkar@ncl.res.in

Abstract:

The fascination with space and human spaceflight has significantly increased in recent years. Nevertheless, microgravity has a significant impact on humans. Immune and red blood cells utilize hematic or lymphatic streams (bio-fluid) as their primary mode of transport, and these streams have been identified as a significant concern under microgravity. This study aims to quantitatively address the puzzle of how cells are influenced by gravity when they are suspended in bio-fluid. The Dissipative Particle Dynamics (DPD) approach was used to model blood and the cell by applying gravity as an external force along the vertical axis and varied from 0g to 2g during parameter sweeps. It was observed that the cell undergoes shape change and spatially aligns under the influence of gravity, and this was quantified with metrics such as Elongation and Deformation indices, pitch angle, and normalized center of mass. The Elongation Index and the normalized center of mass declined linearly with the applied gravity. Correlation analysis showed a strong correlation between applied gravity and the aforementioned variables. Forces exerted on the solid, specifically drag, shear stress, and solid forces, declined in magnitude as the gravitational force exerted on the cell was

increased. Further analysis showed that increasing gravity affected the cell's velocity, leading to extended proximity near the wall and increased viscous interaction with the surrounding fluid particles, triggering a shape change. This study marks a significant step in understanding gravity's effects on blood cells.

Keywords: Altered gravity, Red Blood Cell, fluid flow, Dissipative Particle dynamics, computational modeling.

1. Introduction:

In recent years, there has been a significant surge in the intrigue around space and human spaceflight. This is evident through the establishment of the Artemis Accord, which signifies humanity's intention to dispatch personnel to both the Moon and Mars during the timeframe of the 2030s [1], necessitating an extended stay in hostile environments. However, previous studies have reported various physiological changes in astronauts who have spent extended periods in the International Space Station (ISS). These changes include heightened allergic reactions, decreased counts of T- and B-cells, impaired morphology and activation of immune cells [2], reduced activity of macrophages [3,4], and inconsistent release of interleukins and chemokines [4–6]. Given the potential health risks associated with space exploration, it is essential to conduct a thorough investigation into the influence of gravity on the immune and associated systems to ensure the well-being of humans in future space missions.

The effects of microgravity (10^{-6}g; g = 9.81 m/s^2) on the human body have been thoroughly studied, with body fluids recognized as a significant source of concern. Prisk [7] states, body fluids collect in the thorax before redistribution and eventual balance. While immune cells can be found as resident cells in tissues, their primary mechanism of movement to their site of action is via hematic or lymphatic streams [8]. Several studies have related the absence of convection to the lack of driving forces in microgravity (except capillary force). The lack of convection reduces shear pressures [9], cell sedimentation [10], nutrient delivery, and waste elimination [11], resulting in decreased gene expression and subsequent physiological consequences [9,12]. Prior studies have suggested that these factors contribute to the immune system's

impairment and, as a result, a decrease in immunological activity. Therefore, understanding the association between cellular mechanics and mechanotransduction in microgravity is critical to solving the immune dysfunction puzzle. Microgravity research has primarily focused on experimental procedures, and studies have been done from a mechanics perspective on vesicles and RBCs [13–15] under microgravity. Similarly, some computational studies have been done on non-adherent cells such as stem cells [16] and bone/osteocytes [17–20]; their underlying biology has not been investigated.

The mechanism through which cells perceive gravity remains a puzzle. While certain structures like the Otolith in the ears are confirmed to play a role, the exact process by which non-adherent cells sense gravitational forces, especially in conjunction with shear forces in fluid suspension, remains uncertain. Questions linger regarding whether these cells uniformly sense gravity across their surfaces or if specialized structures on their surfaces are involved. If direct sensing occurs, is there a specific point of contact inside the cell to transmit this force? Alternatively, if a protein on the cell surface mediates this process, what kind of structural change enables it to relay signals internally? Additionally, the unclear understanding of how cells respond to mechanotransduction under conditions of microgravity and shear further complicates the picture. These questions are an unresolved topic on the complex interplay between physics (microgravity, forces, and cellular morphology), biology (gene regulation), and chemistry (small molecule production), underlined in a recent review [21].

In this study, we have developed a numerical model using Dissipative Particle Dynamics (DPD) to explore how red blood cells (RBCs) behave under various gravitational conditions. The current model links the fluid movement with solid structures

by employing DPD-based force equations. Through this method, we aimed to address broader questions about how cells change shape and respond to shifts in gravity. The simulated cell displayed behavior akin to what is observed in experiments, where gravity influenced the cell's movement. Primary objective of this study is to investigate alterations in cell shape caused by external forces and pinpoint the factors affecting these changes using metrics like the Elongation Index, Deformation Index, pitch angle, and normalized center of mass. We aimed to elucidate the shifts connected with these metrics. Additionally, we delved into how solid forces such as drag, shear stress, and other mechanical forces impact cell behavior in response to gravity. The results imply that forces are influenced by cell migration speed, interaction with surrounding fluids, and the magnitude of applied gravity. Our findings collectively elucidate how cells respond to varying gravitational forces, detailing their movement, interactions with vessel walls, and the often challenging-to-measure forces they experience during these processes in experiments.

2. Material and methods:

This section provides a concise overview of the dissipative particle dynamics (DPD) formulation with a two-dimensional discrete cell model of red blood cells (RBC).

2.1. Bio-Fluid model:

DPD is a mesoscopic scale simulation technique initially proposed by Hoogerbrugge and Koelman [22] that utilizes particles as its fundamental representation units. The forces exerted on the particle are determined by evaluating the pairwise

distances between particles within a specified cut-off radius. The DPD method computes three internal forces for each particle while exerting an external force on each particle. Newton's second law provides a framework for understanding the temporal progression of forces,

$$\frac{dr_i}{dt} = v_i, \qquad m_i \frac{dv_i}{dt} = F_{internal} + F_{external} \tag{1}$$

Where r_i and v_i are the position and velocity vectors of particle i, and the unit of mass is taken to be the mass of a particle. $F_{Internal}$ is the internal forces generated due to pairwise interactions between particles. Internal forces can be categorized into three types: conservative force (F^C), dissipative force (F^D), and random force (F^R). Conservative force is a linear soft repulsive potential; dissipative force is a viscous force to mimic viscous friction, and the random force accounts for the Brownian motion at the meso- and microscopic scale.

$$F_{internal} = \sum_{i \neq j}^{N} F^C{}_{ij} + F^D{}_{ij} + F^R{}_{ij} \tag{2}$$

$$F^C{}_{ij} = \alpha_{ij}\, w^C(\overrightarrow{r_{ij}})\, \widehat{r_{ij}} \tag{3}$$

$$F^D{}_{ij} = -\gamma_{ij}\, w^D(\overrightarrow{r_{ij}}) < \overrightarrow{v_{ij}}, \widehat{r_{ij}} > \widehat{r_{ij}} \tag{4}$$

$$F^R{}_{ij} = \sigma_{ij}\, w^R(\overrightarrow{r_{ij}})\, \xi_{ij} \left(\frac{1}{\sqrt{dt}}\right) \widehat{r_{ij}} \tag{5}$$

The strength of dissipative and random forces is represented by the dissipative strength parameter (γ_{ij}) and the random strength parameter (σ_{ij}), respectively. The soft repulsive potential (**Eq. 3**) and conservative force coefficient (α_{ij}), keep interacting particles from getting too near to one another. r_{ij} is the distance between particle i and j, $\widehat{r_{ij}}$ is its unit vector, and $< \overrightarrow{v_{ij}}, \widehat{r_{ij}} >$ is the dot product of the unit vector and velocity

difference between particle i and j. ξ_{ij} is a random number following zero mean and unit variance and has the following properties.

$$< \xi_{ij}(t) > = 0 \tag{6}$$

$$< \xi_{ij}(t)\, \xi_{kl}(t') > = (\delta_{ik}\delta_{jl} + \delta_{il}\delta_{jk})\, \delta(t - t') \tag{7}$$

The random number applied to a pair of particles is kept constant to preserve momentum. Interparticle-dependent weight parameters w^C, w^R, w^D vanish at $\overrightarrow{r_{ij}} > r_c$. These weight parameters are as follows

$$w^C = (1 - \overrightarrow{r_{ij}}/r_c), when\ \overrightarrow{r_{ij}} > r_c, else\ 0 \tag{8}$$

$$w^R = (1 - \overrightarrow{r_{ij}}/r_c)^k, when\ \overrightarrow{r_{ij}} > r_c \tag{9}$$

$$w^C = (w^R)^2, when\ \overrightarrow{r_{ij}} > r_c \tag{10}$$

Groot and Warren [23] found a relationship between the dissipative strength parameter, random strength parameter, and the fluctuation-dissipation theorem given by,

$$\sigma^2 = 2\gamma kBT \tag{11}$$

kBT stands for the system temperature. As the random force tends to "heat up," while the dissipative force seeks to cause viscous damping in the system, doing so will guarantee the temperature stability of the system. The corresponding dissipative and random parameter in **Eq. 11** explains how the two forces work as a thermostat in this way.

Boundary conditions:

Similar to Fan et al. [24], to implement the no-slip boundary condition, particles that penetrate the wall layer are reflected back into the simulation domain, whereby their velocity is reassigned from a normal distribution. Cartesian coordinate system is chosen as a frame of refence, with x-direction along the horizontal and the y-direction along the

vertical axis (shown in **Fig. 1**). The direction of reflection is determined by the vector 'n', which is orthogonal to the boundary. The periodic boundary condition is enforced in the x-direction.

$$v_x = v_{random} \tag{12}$$

$$v_y = v_{random} + n(\sqrt{(nv_{random})^2} - nv_{random}) \tag{13}$$

Parameter scaling:

DPD simulation is carried out in reduced units. In order to scale parameters, defining the reference parameters becomes necessary. In this study, the physical reference length and cut-off radius (r_c) are $1x10^{-6}$ m; in DPD terms, r_c equals 1. Particle density (ρ_{DPD}), reference temperature (T), reference time (t_{ref}), reference velocity (v_{ref}), and Young's modulus of RBC are additional reference parameters required to execute the DPD simulation. The **Supplementary Information, Section 1, Parameter derivation,** provides the derivation of simulation parameters.

2.2. Cell model:

The mean diameter of a human RBC ranges from 6.10 to 8 micrometers. When fully developed, it assumes a biconcave morphology and exhibits an absence of a cellular nucleus. The structure of RBCs consists of phospholipid bilayers and the cytoplasm. Of which the cytoplasm can be described as a viscous Newtonian liquid. The cytosol preserves the internal volume and uniformly disperses external pressures exerted on its surface. The RBC membrane consists of a spectrin network interconnected with the cell wall. The structural networks, which govern the general deformation behavior of RBCs, constitute most of the load-bearing framework of RBCs. The overall shape is determined by various factors, including the cell membrane's

elasticity, surface area, and the volume enclosed within the cell. Thus, RBCs possess a certain degree of flexibility, like a partially inflated capsule, and that shape can be used to model it.

In this study, RBC is modeled as a ring of 76 finite-sized DPD particles interconnected by non-linear Worm Like Chain (WLC) springs. Multiple studies have employed different numbers of particles (ranging from 10 to 88) to simulate RBC [25–28]. However, the present formulation is similar to Pan et al. [25]; the spring is modeled as a worm-like chain (WLC), and an area penalty function is applied to conserve the RBC shape and area [27]. RBC initially starts as a circle with a radius of $3.05r_c$; applying the area penalty function forces the RBC to settle to its minimum energy shape. The energy functions are presented below:

$$E_{WLC} = \frac{kBT\, L_m}{4p}\left(\frac{3x^2 - 2x^3}{1 - x}\right) \tag{14}$$

E_{WLC} represents elastic energy stored by a spring described by a non-linear relation, where kBT is the system temperature, L_m is the maximum permissible length of the spring, p is the persistence length of the flexible spring, and x is the ratio L_j/L_m, where L_j is the spring's current length. Similarly, to account for the membrane's bending and compressional stiffness. A three-point interaction potential (E_{bend}) is applied where k_b is the RBC membrane bending constant, and θ_{ijk} is the instantaneous angle between the two consecutive springs with the jth particle as the center.

$$E_{bend} = k_b(1 - cos(\theta_{ijk})) \tag{15}$$

To maintain shape and conserve the internal, we apply the area penalty function as a potential,

$$E_{area} = \frac{k_a}{2}\left(\frac{A - A_0}{A_0}\right)^2 \tag{16}$$

Where k_a is the area coefficient, A is the instantaneous area, and A_0 is the intended area of RBC. The reduced area parameter is introduced to define the intended enclosed area, and the relationship is given by $s = \frac{4A_0}{\pi Dia_{RBC}{}^2}$. The total energy of the system and the forces is given by

$$E_{Total} = E_{WLC} + E_{bend} + E_{area} \tag{17}$$

$$F_i = -\frac{\partial(E_{WLC} + E_{bend} + E_{area})}{\partial r_i} \tag{18}$$

The values of the parameters described above are shown in **Table 1**.

Table 1: List of all physical parameters used in the DPD simulation

Parameter	Value	SI unit	Reference
Shear modulus (G)	5	**μN/m**	*[29,30]*
Young's modulus (Y)	14.999	**μN/m**	***Derived (Y = 2G(1+v))***
Poisson ratio (ν)	0.4999	**-**	**-**
Number density	4	**-**	***Assumed***
Reference temperature	310	**K**	***Assumed***
Reference velocity	0.01	**mm/s**	***Derived***
Reference time	0.088	**s**	***Derived***
kBT*	0.125	**-**	***Derived***

kb	50*kBT	**N*m**	*[31,32]*
ka	10e-6	**N/m**	*[26]*
Persistence length (l_p)	0.0067e-6	**m**	*[26,33]*
L_m	0.40	**-**	***Derived***
RBC	76	**Particles**	***Assumed***
Fluid	16238	**Particles**	***Assumed***
Reduced area parameter (s)	0.481	**Dimensionless**	*[26]*
dt	0.001	**-**	**-**

Computational details and Benchmarking:

The parametric study of fluid flow and structure interaction is conducted at a physiological temperature of 310 K, which is equivalent to 0.125 in DPD units, corresponding to the average temperature of the human body, and a cutoff radius of 1 (DPD units), representing a microscopic dimension. The simulation is established and populated with particles, resulting in a particle density of ρDPD = 4.0. A simulation box with dimensions of $204r_c$ x $20r_c$ is utilized, with periodic boundary conditions (PBC) to allow the flow of particles and reflection with repulsion implemented at the walls to mimic the no-slip condition. The particles are initialized with random values for velocity and acceleration. The DPD system can be classified as an NVE (Particle, Volume, and

Energy) ensemble, in which the three entities are conserved and system temperature is monitored for fluctuation. The minimized RBC shape, as depicted in **Fig. 1**, is positioned at the center of the left boundary. The fluid particles contained within the RBC are regarded as the RBC cytosol. In order to induce flow, a minor external force is applied to the system in the x direction, and to mimic gravitational conditions, another eternal force is applied in the y direction representing gravity. The dissipative strength parameter (γ_{ij}) is chosen to be 4.5, and the random strength parameter (σ_{ij}) is calculated to be 0.795 based on the relation in **Eq. 11**. The Conservative force coefficient (α_{ij}) is considered 2.34 based on the following relation $\frac{75kBT}{\rho_{DPD}}$ given by Groot and Warren [23].

Simulations were performed for 25 seconds in the physical scale, with a timescale equivalent to 0.088 sec and a time step size of order O(10^{-3}). An in-house Python-based code was developed to implement a two-dimensional model for blood flow, and data analysis was carried out in MATLAB 2020a. The interaction characteristics pertaining to various types of particles are presented in **Table 2**.

Table 2: DPD interaction parameters

Parameters	Fluid - Fluid	Solid -Solid	Fluid - Solid
α_{ij}	$\frac{75kBT}{\rho_{DPD}}$	27.5	$\sqrt{a_{ff} * a_{ss}}$
γ_{ij}	4.5	4.5	4.5
σ_{ij}	$\sqrt{2\gamma_{ij}kBT}$	$\sqrt{2\gamma_{ij}kBT}$	$\sqrt{2\gamma_{ij}kBT}$
$\boldsymbol{r_c}$	1.0	1.0	1.0

Statistical analysis:

The data and subsequent statistical analyses were performed utilizing MATLAB® 2020 software. Evaluation of cell morphology and spatial alignment involved fitting normal probability distribution functions to the aggregated data using the fitdist package. Hypotheses regarding the potential differences in the median values of parameters including EI, DI, theta and YCoM between the 1g sample and both micro- () and hypergravity samples were assessed via two-sided nonparametric test (Mann-Whitney U test, ranksum package), employing a dataset comprising 5112 samples from 6 simulation runs for each gravitational condition. Significance levels were designated as $p < 0.05$, $p < 0.01$ and $p < 0.001$ to denote statistical significance between the compared samples.

3. Results and discussions:

***RBC mechanics*:**

A stretch test is performed to evaluate RBC's structural integrity and mechanical properties of RBC. In this study, we follow the protocol laid out by Dao et al. [34]. RBC is affixed to a silica bead at one extremity and subjected to incremental force to induce displacement from the opposing end. This test enables the assessment of its strength and the extent of deformation that may arise due to external forces. The variations in axial and transverse diameter are measured and graphed in relation to the applied force (**Fig. 2(A)**). These measurements are then compared to the findings of Bohiniková et al., Fedosov et al., and Suresh et al. [33,35,36]. The present simulation agrees with the

experimental result and the 3D simulations. Similarly, we compare the changes in RBC shape during the optical tweezer test of Zhang and Liu (refer to Figure 3(c)) [37] at specific force intervals **(Fig. 2(B))**. The shape change observed in our simulation is comparable to the shape produced during the experiment. Based on the agreement of the results, parameters used during the stretch test were used in the DPD simulation.

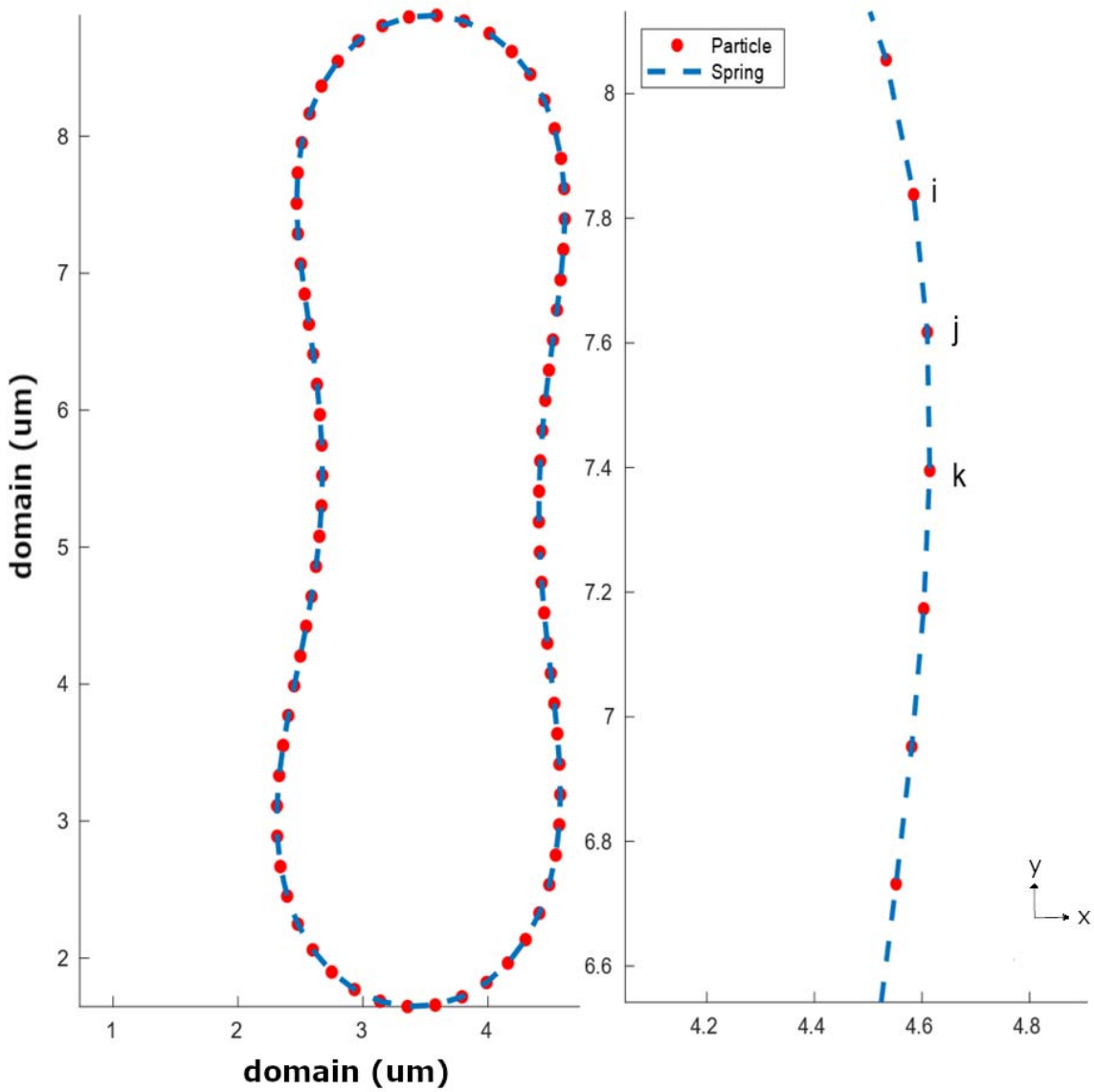

Fig. 1: (a) Minimum energy shape of RBC when the reduced area parameter is applied. (b) Nodes i, j, and k are connected by a spring of length l_0 at rest and the

intersection of two adjacent springs, ij and jk, at the junction point j subtends angle θ_{ijk}.

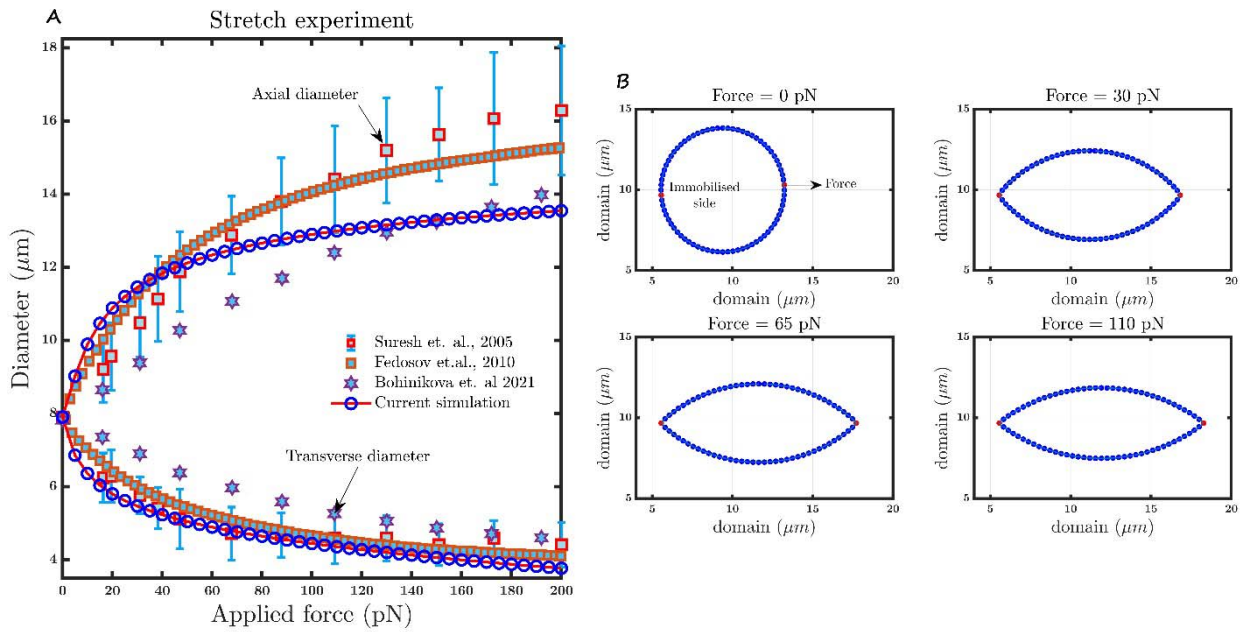

Fig. 2: (A) Axial and transverse diameter of the RBC when deformed with external stretch force, Current (blue circle) compared to Suresh et al., [35] **experimental test, Bohiniková et al.,** [36] **and Fedosov et al. 's** [33] **3D simulation results. (B) Shapes produced at specific force intervals in the optical tweezer test closely resemble Zhang and Liu's optical tweezer test** [37]**.**

Cell dynamics and parametric sweep:

To investigate the interactions between fluids and solids at the mesoscale, the cell was energy-minimized and then placed at the start of the fluid domain, which had previously reached a state of equilibrium. With the introduction of RBC into the system, a spike in temperature was observed, eventually stabilizing near the equilibrium kBT value. Once systemic equilibrium with the RBC is achieved, the cell experiences forces, such as shear and drag, from the surrounding fluid. To explore the impact of gravity on cellular behavior, gravity was introduced as an external force along the y-axis and varied from 0g (< 1g - microgravity regime) to 2g (> 1g - hypergravity regime) in an increment of 0.25g. The system was simulated over a 25-second timeframe on the physical scale.

The computational domain was segmented into 400 bins in the y-direction for further analysis to calculate rheological and cell-dependent properties. Local flow parameters were determined by averaging each bin's sampled data from the last 25% of the data.

It was observed that, over time, due to the interaction with the surrounding fluid, RBCs transitioned from a biconcave shape to various configurations, such as those resembling a symmetric parachute, slipper, asymmetric parachute, or anti-parachute. The aforementioned configurations that RBC assumed were contingent upon its location within the given domain. In order to determine the transient shape change, two distinct parameters were introduced, namely the elongation index and the deformation index, derived from the Gyration tensor which are expressed as follows:

$$G_{mn} = (\frac{1}{\mathrm{N}})\Sigma((\mathrm{r}^{\mathrm{i}}{}_{\mathrm{m}} - \mathrm{r}^{\mathrm{c}}{}_{\mathrm{m}})(\mathrm{r}^{\mathrm{i}}{}_{\mathrm{n}} - \mathrm{r}^{\mathrm{c}}{}_{\mathrm{n}})) \tag{19}$$

The notation $r^{i}{}_{m}$, $r^{i}{}_{n}$ denotes the current position of the solid vertex (particle) and $r^{c}{}_{m}$, $r^{c}{}_{n}$ represents the center of mass of the solid in the x and y directions, respectively. The gyration tensor is a 2 x 2 tensor; diagonalizing the tensor gives two eigenvalues, λ_1 and λ_2. These eigenvalues represent the cell diameter along the x and y directions. Assuming, $\lambda_1 > \lambda_2$, the ratio of these eigenvalues gives,

$$EI = (\frac{\lambda_1}{\lambda_2}) \tag{20}$$

$$DI = (\frac{\lambda_1 - \lambda_2}{\lambda_1 + \lambda_2}) \tag{21}$$

To analyze the impact of the surrounding fluid and gravity on a cell, drag, shear, and acceleration acting on a solid object were calculated based on Chen et al.'s [38] formulation.

$$F_D = \frac{1}{2} C_D A_{RBC} \rho_{DPD} |U| U \tag{22}$$

$$C_D = \frac{24}{Re}(1 + 0.150Re^{0.681}) + \frac{0.407}{1 + 8710/Re} \tag{23}$$

$$Re = (\frac{2\rho_{DPD}||U_{solid}||L}{\eta}) \tag{24}$$

$$\eta = \frac{315kBT}{128\pi\gamma r_c^3} + \frac{512\pi\gamma\rho_{DPD}^2 r_c^5}{51975} \tag{25}$$

In this context, F_D represents the drag force, C_D denotes the drag coefficient, $\boldsymbol{A_{RBC}}$ signifies the area enclosed by RBC, $\boldsymbol{\rho_{DPD}}$ represents the system's density, and U denotes the RBC's velocity. Viscosity ($\boldsymbol{\eta}$) was estimated using the methodology outlined in Fan et al. [39] to calculate the drag coefficient. Eq. 23 establishes a scaled correlation between the Reynolds number (ratio of inertial to viscous forces) and the drag coefficient; Brown and Desmond [40] established a correlation by analyzing sphere drag data collected over the twentieth century, valid for Reynolds numbers below 100,000. The calculated values were compiled and categorized based on temporal and parametric variables (presented in **Fig. 3** and **Supplementary Information, Section 2, Fig. S1-S8**).

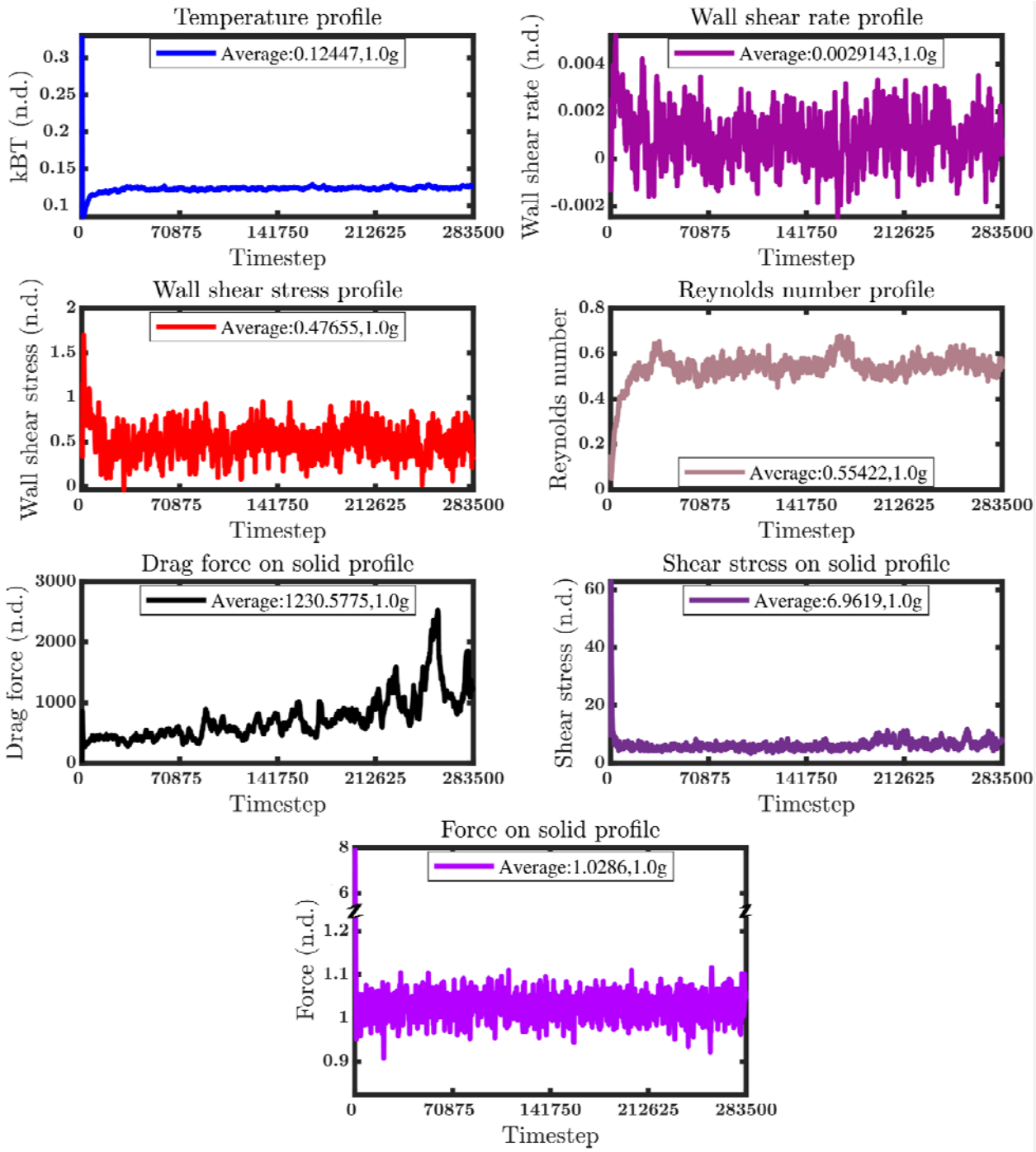

Fig. 3: The temporal evolution of fluid and solid parameters at 1g; value averaged for the last 25% of data. Initially, there are observed fluctuations in several parameters, which gradually stabilize to equilibrium. The drag force acting on the solid object exhibit an initial range bound stabilization and increases as the cell began interacting more with the surrounding fluid particles.

Furthermore, the pitch angle and normalized the longitudinal center of mass of the cell were monitored in addition to assessing elongation and deformation indices. The phenomena of elongation and deformation indices offer insights into the alterations in shape resulting from the contact between a fluid and a solid. The former two can be utilized to assess the physical changes that impact the cell due to gravitational changes. Time-dependent variations of all the previously mentioned indices are presented in **Fig. 4**.

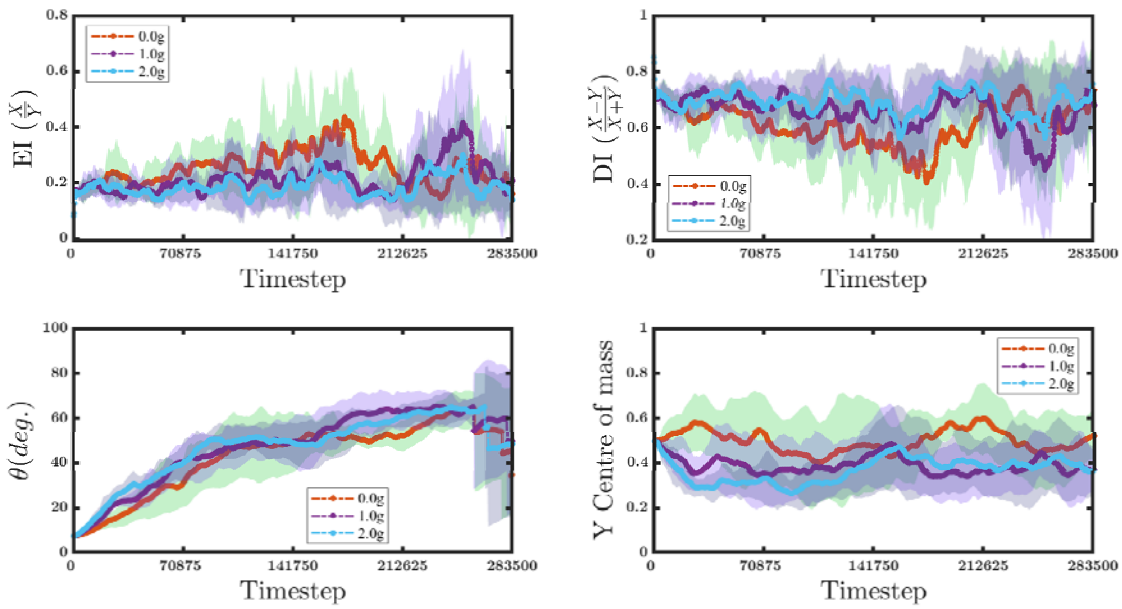

Fig. 4: The evolution of solid parameters throughout time. A) Comparison of RBC elongation indexes at 1g, 0g, and 2g. B) A comparison of RBC deformation indices at 1g, 0g, and 2g. C) A comparison of RBC pitch angles at 1g, 0g, and 2g. D) A comparison of the Y center of mass at 1g, 0g, and 2g.

In **Fig. 4**, it is evident that the cell subjected to higher gravity (hypergravity in comparison to 1g) exhibits subdued elongation, rapid shift in pitch angle, and movement toward the bottom wall of the domain. Conversely, the cell exposed to reduced gravity (microgravity) experienced the opposite effects. While it is possible to derive specific insights by examining the temporal fluctuations of these indices, however the

application of the random force induces stochasticity in the system, contributing to noise in the temporal scale. Therefore, to comprehensively derive an understanding of the temporal behaviors, aggregation of data becomes necessary to identify fundamental distribution patterns. Hence, to ascertain the distribution and likelihood of these quantitative metrics, probability histograms were constructed, and theoretical distributions were fitted over the probability histogram data (**Fig. 5 and 6, Supplementary Information, Section 2, Fig. S9 and S10**). Various theoretical distributions were used to fit the constructed histograms. Among them, the normal distribution fit was able to explain few of the histograms, but majority of the histograms did not follow normal distribution. Therefore, subsequent hypothesis testing employed a non-parametric approach to avoid assumptions about the underlying distribution.

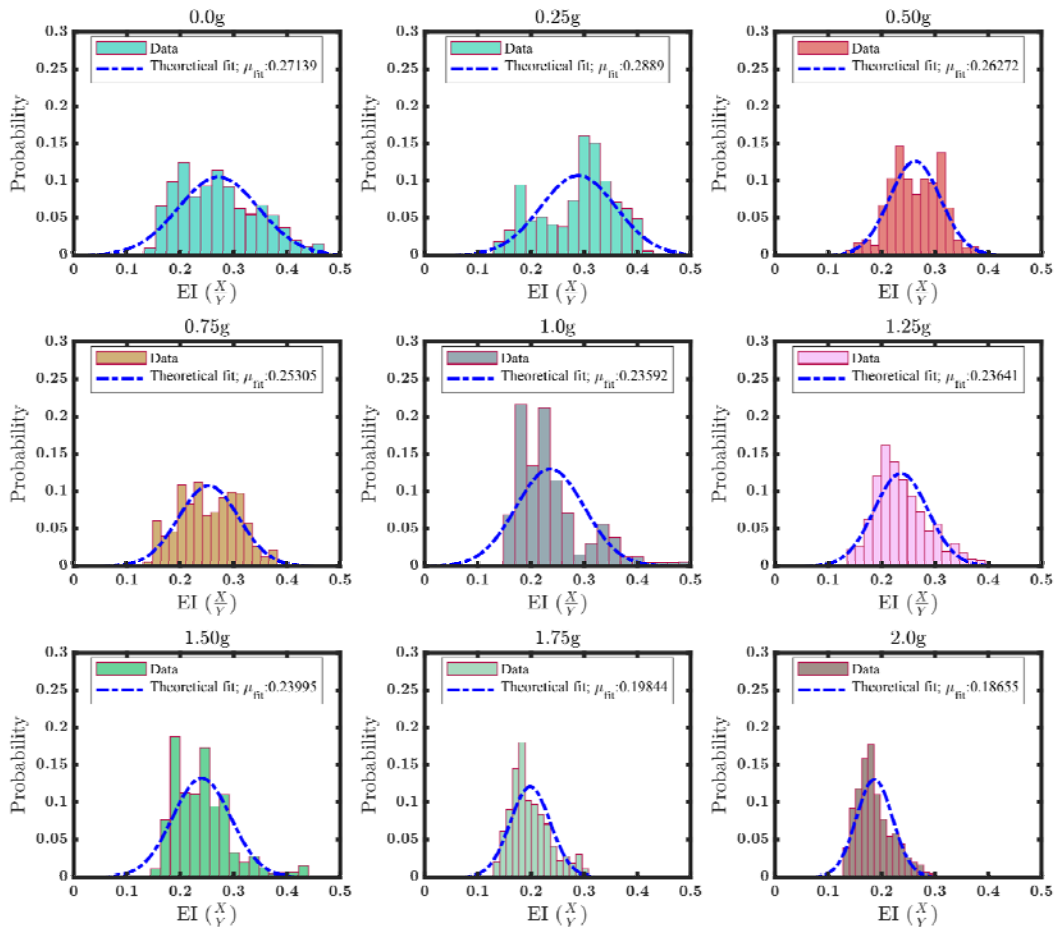

Fig. 5: The probability distribution of the Elongation Index data and the fitted theoretical distribution over EI data. Mean reduces as the gravity decreases from 1g and, conversely, increases as the gravity condition increases.

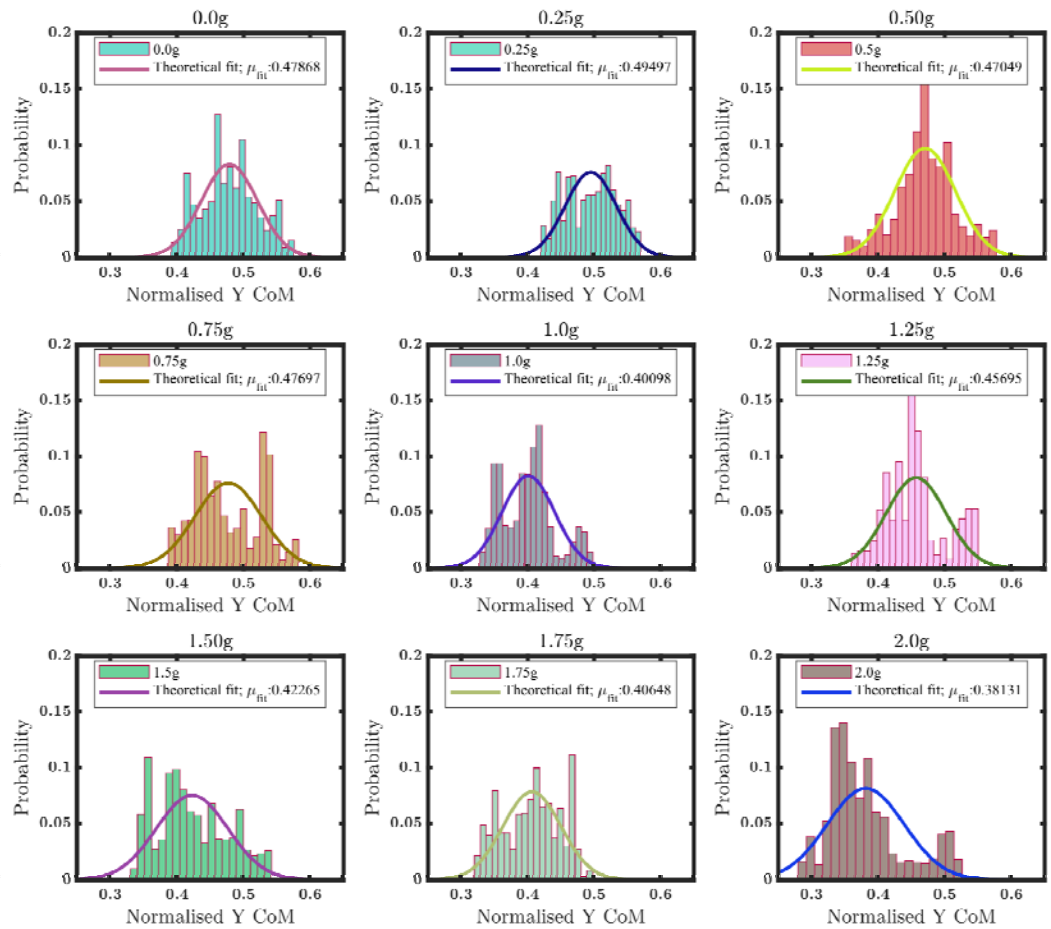

Fig. 6: The probability distribution of the normalized Y center of mass data and the fitted theoretical distribution over it. Comparing the mean of the distribution of 1g to the mean under other gravity conditions, the mean increases as the gravity decreases from 1g and decreases as the gravity condition increases.

The Mann-Whitney U test was conducted to validate the findings by aggregating 5112 samples for each gravitational group. We assumed the null hypothesis for the Mann-Whitney test to show no difference between the median of 1g and the tested gravitational condition. For the alternate hypothesis, the medians between the tested groups were supposed to be different. Significance levels were designated as $p < 0.05$, $p < 0.01$, and $p < 0.001$ to denote statistical significance between the compared samples.

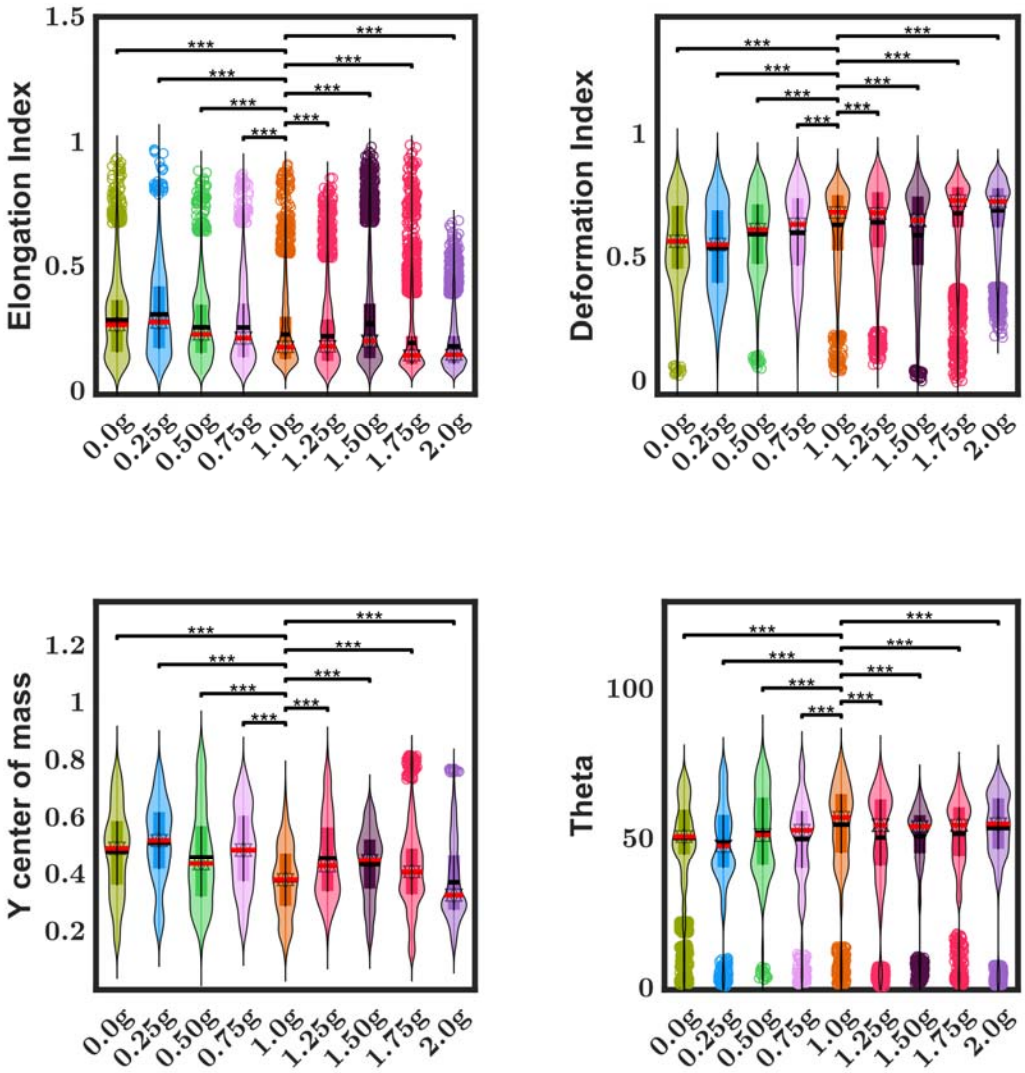

Fig. 7: The variation of Elongation Index (EI), Deformation Index (DI), Theta, and Y center of mass (YCoM) among the samples of 1g and other gravitational conditions assessed through the Mann-Whitney U test. The violin plot illustrates the data distribution, with the red bar representing the sample median and the black bar indicating the mean. EI, DI, Theta, and YCoM in the 1g sample are distinct compared to those in the 0g and 1g samples. (*p < 0.05, **p < 0.01, ***p < 0.001)

Fig. 7 compares the median values of EI, DI, Theta, and YCoM at 1g with those at other gravitational conditions. A noticeable difference in medians is observed between 0g and 2g conditions. However, a minimal disparity is observed in the central values of EI and

DI during the initial stages of the hypergravity regime (e.g., 1.25g and 1.50g). Furthermore, substantial differences are evident in the central values across all gravitational conditions in the Theta and YCoM variables, as indicated by the confidence levels provided by the p-value. These findings support the alternate hypothesis, suggesting that gravitational variations induce changes in cell shape and facilitate spatial alignment in response to applied gravity.

In **Fig. 5**, while maintaining the mean of 1g distribution as a reference point, we assess the variation in the mean values. From the means of probability distribution plots, it is evident that the Elongation Index exhibits a linear relationship with the magnitude of gravitational force applied, starting from 0g to 2g. In order to provide additional verification, a linear regression model was employed. The coefficient of determination, denoted as R^2, is calculated to be 0.8718 (**Fig. 8(A)**), suggesting that the model effectively describes the dataset. Moreover, the Pearson correlation coefficient was computed at -0.9337, suggesting a robust negative linear association between the observed data. A similar approach was employed for DI, theta, and normalized Y center of mass (YCoM). It is worth noting that the normalized Y center of mass exhibited a linear correlation with the magnitude of gravitational force applied, and their relationship was observed to be the same as that of the Elongation Index. The R^2 for the fit was determined to be 0.7934 (**Fig. 8(B)**). The Pearson correlation coefficient was also calculated to be -0.8907, indicating a strong negative linear relationship between the observed data.

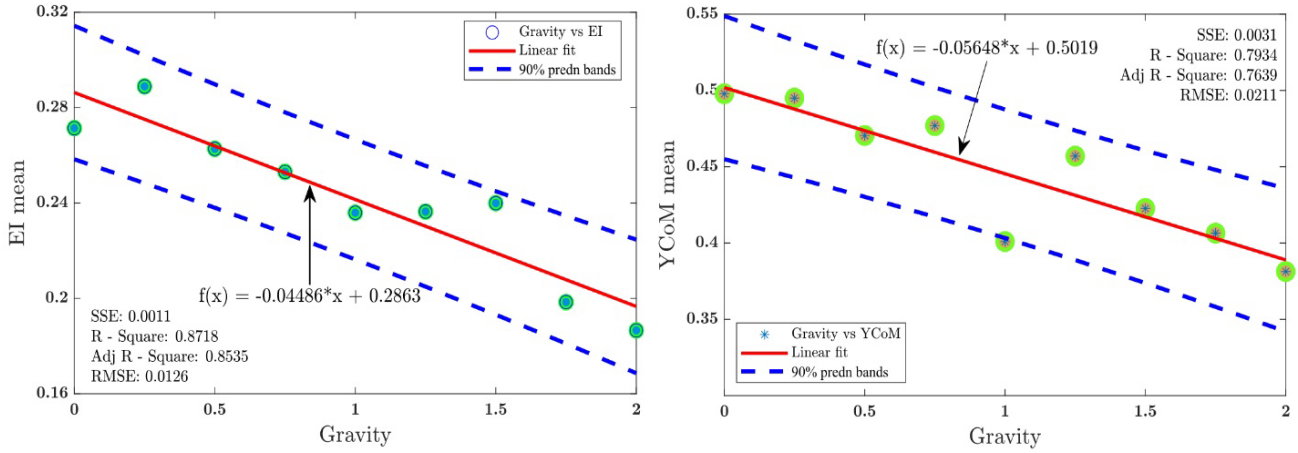

Fig. 8: (A) Linear regression of mean distribution of EI with gravity. Fit shows a strong negative correlation between EI and applied gravity. (B) Linear regression of mean distribution of YCoM with gravity. Fit shows a negative correlation between YCoM and applied gravity.

In addition to the temporal aggregation of solid forces (as shown in **Fig. 4**), parametric aggregation was performed; as illustrated in **Fig. 9**, a decrease in all three forces was observed during the hypergravity regime. In contrast, an increase was detected during the microgravity regime, with the most considerable increase occurring under the 0g condition. Upon reexamining **Eq. 22 to 25**, it becomes apparent that the magnitude of the drag force is dependent on the drag coefficient, which in turn is controlled by Reynold's number. The Reynolds number is dependent on the magnitude of velocity. Velocity is a resultant quantity determined by the rate of change of an object's acceleration, controlled by internal and external forces. The applied gravity is an external force acting in the y-direction with negative signage. It becomes clear that the external application of gravitational force becomes a subtractive force on the fluid and the solid, thereby decelerating it at higher g-levels.

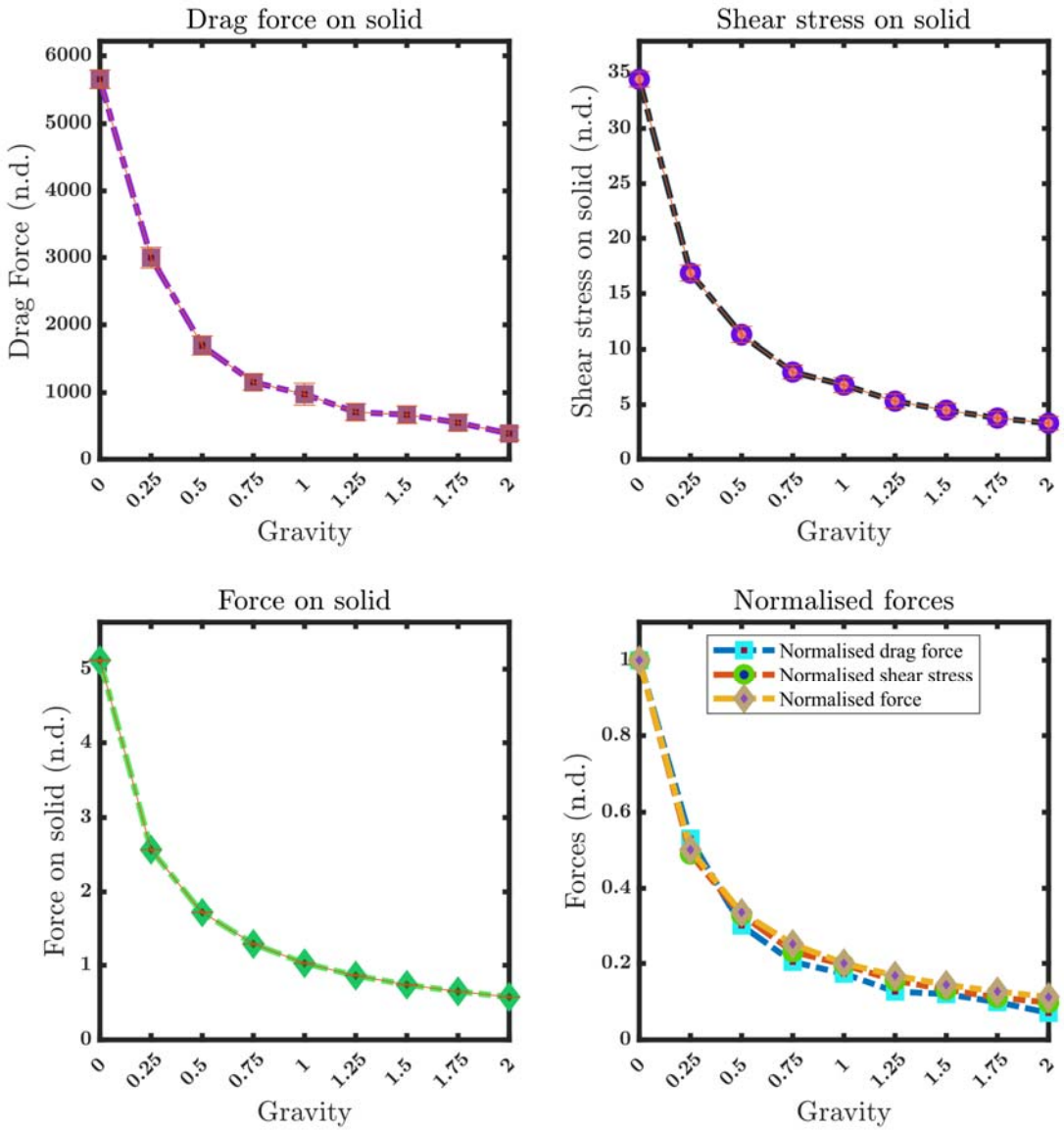

Fig. 9: Parametric variation of Drag, Shear stress, and Solid forces. All three forces increase under microgravity and decrease under hypergravity.

This study examined gravity's impact on cells suspended in the bio-fluid medium. While previous research has explored the cellular interactions at the mesoscopic level using simulation [31,33] and experimental approaches [41,42], the present study represents a novel investigation into the impact of gravitational conditions on cell morphology, distribution, and the corresponding forces. Previously, there have been

some computational studies on the effects of microgravity on osteoclasts [43]; however, there are no computational studies involving cells such as RBC and WBC in micro- or hypergravity regimes. Nevertheless, significant experimental advancements have been made on the impact of microgravity on vesicles and RBCs [13–15]. To corroborate the results of our investigation, a comparative analysis was carried out between the detachment and lift of the RBC and vesicles under the 1g condition of Losserand et al. [44] (refer to Figure 1(c)) with the present work. This study's findings are consistent with the experimental data of the cell behavior near the wall (**Fig. 10: 1g**).

As the cell approaches the wall, it experiences a lift force that results in its displacement away from the wall and towards the centerline. This results in a separation between the walls and the cell, commonly referred to as the cell-free layer. However, in the context of zero gravity, it was observed that the cell moved toward the wall even in the absence of gravitational forces and then pushed the cell with a greater upward force, enabling the formation of stable cell structures along the domain centerline (as depicted in (**Fig. 10: 0g**). In contrast, cells subjected to a gravitational force of 2g exhibit a significant proximity to the wall for longer durations, as depicted in **Fig. 10: 2g**. This phenomenon arises due to increased interaction with the nearby fluid particles, resulting in heightened viscous and dissipative forces. Consequently, the cell experiences a deceleration, thereby reducing drag, shear, and solid forces. Cell’s movement toward the domain wall also triggers the cells to change shape to accommodate the higher force near the wall.

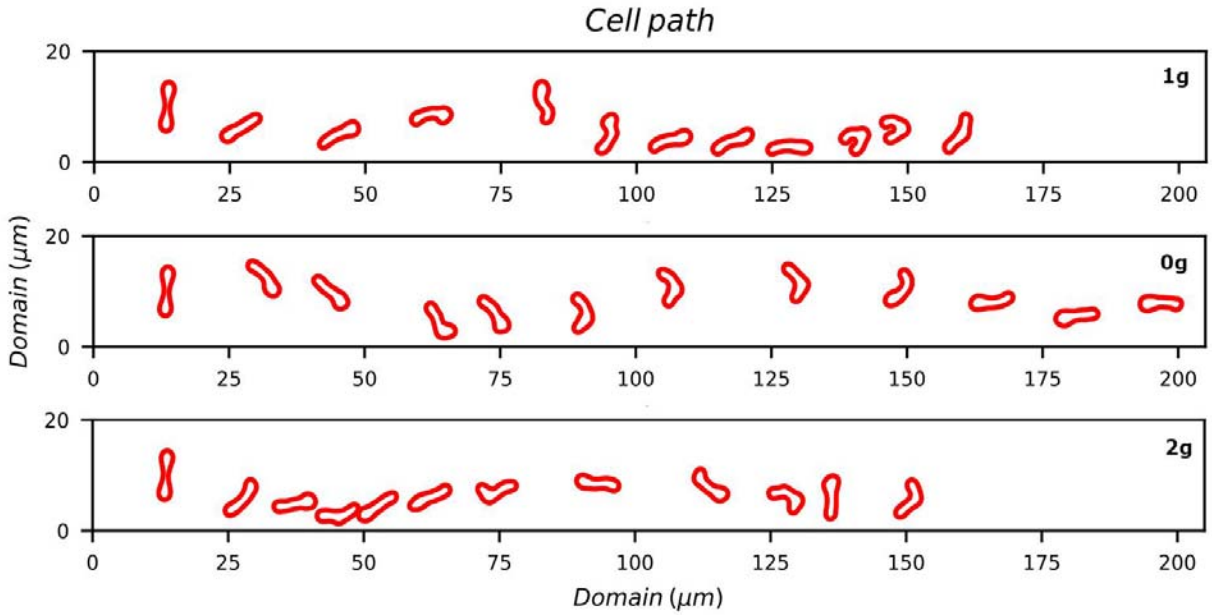

Fig. 10: Distribution of the cell across the domain at selected g-conditions. Although the cell-free layer is formed at all three conditions, it is more pronounced under 0g with the cell pushed to the centerline due to higher lift force, whereas the cell under 1g and 2g moves closer to the wall.

4. Conclusion and Future Directions:

This work has focused on the computational modeling of cell mechanics under an external gravitational force using Dissipative Particle Dynamics. Employing a discrete cellular structure model, the investigation revealed partial answers to initial inquiries regarding the cell's response to changing gravitational forces. The findings reveal that RBC undergoes deformation and elongation in response to gravitational variations, with noticeable alterations in measures such as the EI and DI compared to the 1g condition (as indicated by a p-value < 0.001) signifying shape alteration and spatial realignment. At the same time, the normalized center of mass on the y-axis decreased, indicating a downward shift within the blood vessel. Decreasing normalized center of mass raises the question of how different forces are concentrated on the cell.

Solid forces, including drag and shear stress, were scrutinized to answer that. Solid forces include the forces that are exerted on the solid by the fluid within a neighborhood. These forces experience a reduction in their magnitude whenever there is an increase in the gravity of the cell, mainly a reduction of the cell velocity due to its non-adherent nature. Notably, the study illuminated the dynamic morphological transformations of red blood cells (RBCs) from a biconcave shape to various configurations shaped by their spatial orientation and interaction with the surrounding fluid. The findings of this study have important implications for understanding cell mechanics and the physical response of cells to external forces.

Through numerical simulations, this study pioneers exploring microgravity's influence on cells suspended in a bio-fluid. Future endeavors will involve scaling the research to encompass physiologically relevant quantities of RBCs and immune cells and subject them to varying gravity. Thereby offering crucial insights into fundamental cellular behaviors. Further investigations into the specific molecular and biomechanical mechanisms underlying these observed responses will be pivotal for advancing our comprehension of cellular adaptations to varying gravitational environments.

5. Acknowledgements:

RRS acknowledges funding from the Department of Biotechnology, Govt. of India (Sanction Order No. BT/PR35683/BID/7/937/2019, dated 17.12.2020); AM acknowledges CSIR-GATE for Senior Research Fellowship.

6. Author contributions:

AM coding, simulation, analysis, writing; RRS conceived the study, critical analysis, writing, and proofreading.

7. Data and code availability:

Codes and datasets generated during the current study will be available upon request.

8. Competing interest:

The authors declare no competing interests.

9. References:

[1] S. Creech, J. Guidi, D. Elburn, Artemis: An Overview of NASA's Activities to Return Humans to the Moon, in: 2022 IEEE Aerospace Conference (AERO), 2022: pp. 1–7. https://doi.org/10.1109/AERO53065.2022.9843277.

[2] B.E. Crucian, R.P. Stowe, D.L. Pierson, C.F. Sams, Immune system dysregulation following short- vs long-duration spaceflight, Aviat. Space Environ. Med. 79 (2008) 835–843. https://doi.org/10.3357/asem.2276.2008.

[3] I. Kaur, E.R. Simons, V.A. Castro, C.M. Ott, D.L. Pierson, Changes in monocyte functions of astronauts, Brain Behav. Immun. 19 (2005) 547–554. https://doi.org/10.1016/j.bbi.2004.12.006.

[4] M. Moreno-Villanueva, A.H. Feiveson, S. Krieger, A. Kay Brinda, G. von Scheven, A. Bürkle, B. Crucian, H. Wu, Synergistic Effects of Weightlessness, Isoproterenol, and Radiation on DNA Damage Response and Cytokine Production in Immune Cells, Int. J. Mol. Sci. 19 (2018). https://doi.org/10.3390/ijms19113689.

[5] S. Hauschild, S. Tauber, B. Lauber, C.S. Thiel, L.E. Layer, O. Ullrich, T cell regulation in microgravity – The current knowledge from in vitro experiments conducted in space, parabolic flights and ground-based facilities, Acta Astronaut. 104 (2014) 365–377. https://doi.org/10.1016/j.actaastro.2014.05.019.

[6] C.S. Thiel, S. Hauschild, A. Huge, S. Tauber, B.A. Lauber, J. Polzer, K. Paulsen, H. Lier, F. Engelmann, B. Schmitz, A. Schütte, L.E. Layer, O. Ullrich, Dynamic gene expression response to altered gravity in human T cells, Sci. Rep. 7 (2017) 5204. https://doi.org/10.1038/s41598-017-05580-x.

[7] G.K. Prisk, Microgravity, Compr. Physiol. 1 (2011) 485–497.

https://doi.org/10.1002/cphy.c100014.

[8] H.R. Hampton, T. Chtanova, Lymphatic Migration of Immune Cells, Front. Immunol. 10 (2019) 1168. https://doi.org/10.3389/fimmu.2019.01168.

[9] C.A. Nickerson, C.M. Ott, J.W. Wilson, R. Ramamurthy, C.L. LeBlanc, K. Höner zu Bentrup, T. Hammond, D.L. Pierson, Low-shear modeled microgravity: a global environmental regulatory signal affecting bacterial gene expression, physiology, and pathogenesis, J. Microbiol. Methods. 54 (2003) 1–11. https://doi.org/10.1016/s0167-7012(03)00018-6.

[10] J.W. Wilson, R. Ramamurthy, S. Porwollik, M. McClelland, T. Hammond, P. Allen, C.M. Ott, D.L. Pierson, C.A. Nickerson, Microarray analysis identifies Salmonella genes belonging to the low-shear modeled microgravity regulon, Proc. Natl. Acad. Sci. U. S. A. 99 (2002) 13807–13812. https://doi.org/10.1073/pnas.212387899.

[11] N. Guéguinou, C. Huin-Schohn, M. Bascove, J.L. Bueb, E. Tschirhart, C. Legrand-Frossi, J.P. Frippiat, Could spaceflight-associated immune system weakening preclude the expansion of human presence beyond Earth's orbit?, J. Leukoc. Biol. 86 (2009) 1027–1038. https://doi.org/10.1189/jlb.0309167.

[12] S.J. Crawford-Young, Effects of microgravity on cell cytoskeleton and embryogenesis, Int. J. Dev. Biol. 50 (2006) 183–191. https://doi.org/10.1387/ijdb.052077sc.

[13] M.A. Mader, C. Misbah, T. Podgorski, Dynamics and rheology of vesicles in a shear flow under gravity and microgravity, Microgravity - Science and Technology. 18 (2006) 200–203. https://doi.org/10.1007/BF02870409.

[14] N. Callens, C. Minetti, G. Coupier, M.-A. Mader, F. Dubois, C. Misbah, T.

Podgorski, Hydrodynamic lift of vesicles under shear flow in microgravity, EPL. 83 (2008) 24002. https://doi.org/10.1209/0295-5075/83/24002.

[15] T. Podgorski, N. Callens, C. Minetti, G. Coupier, F. Dubois, C. Misbah, Dynamics of Vesicle Suspensions in Shear Flow Between Walls, Microgravity Sci. Technol. 23 (2011) 263–270. https://doi.org/10.1007/s12217-010-9212-y.

[16] R.V. Ghaemi, B. Vahidi, Z. Alihemmati, M.H. Sabour, N. Haghighipour, Finite Element Analysis of the Effects of Microgravity Conditions on Shear-Induced Modulation of Stem Cells, in: 2021 28th National and 6th International Iranian Conference on Biomedical Engineering (ICBME), 2021: pp. 148–153. https://doi.org/10.1109/ICBME54433.2021.9750328.

[17] H.Y. Liu, S. Zhao, H. Zhang, S.Y. Huang, W.T. Peng, C.Q. Zhang, W. Wang, Research on solute transport behaviors in the lacunar-canalicular system using numerical simulation in microgravity, Comput. Biol. Med. 119 (2020) 103700. https://doi.org/10.1016/j.compbiomed.2020.103700.

[18] S. Zhao, H. Liu, Y. Li, Y. Song, W. Wang, C. Zhang, Numerical analysis of the flow field in the lacunar-canalicular system under different magnitudes of gravity, Med. Biol. Eng. Comput. 58 (2020) 509–518. https://doi.org/10.1007/s11517-019-02108-5.

[19] H.Y. Liu, C.H. Zhao, H. Zhang, W. Wang, Q.J. Liu, Simulation study on the effect of resistance exercise on the hydrodynamic microenvironment of osteocytes in microgravity, Comput. Methods Biomech. Biomed. Engin. 25 (2022) 1757–1766. https://doi.org/10.1080/10255842.2022.2037130.

[20] H. Wang, L. Gao, X. Chen, C. Zhang, Study on mass transfer in the bone lacunar-

canalicular system under different gravity fields, J. Bone Miner. Metab. 40 (2022) 940–950. https://doi.org/10.1007/s00774-022-01373-z.

[21] A. Murali, R.R. Sarkar, Mechano-immunology in microgravity, Life Sci. Space Res. 37 (2023) 50–64. https://doi.org/10.1016/j.lssr.2023.03.001.

[22] P.J. Hoogerbrugge, J.M.V. Koelman, Simulating Microscopic Hydrodynamic Phenomena with Dissipative Particle Dynamics, EPL. 19 (1992) 155. https://doi.org/10.1209/0295-5075/19/3/001.

[23] R.D. Groot, P.B. Warren, Dissipative particle dynamics: Bridging the gap between atomistic and mesoscopic simulation, J. Chem. Phys. (1997). https://pubs.aip.org/aip/jcp/article-abstract/107/11/4423/478600.

[24] X. Fan, N. Phan-Thien, N.T. Yong, X. Wu, D. Xu, Microchannel flow of a macromolecular suspension, Phys. Fluids . 15 (2003) 11–21. https://doi.org/10.1063/1.1522750.

[25] W. Pan, B. Caswell, G.E. Karniadakis, A low-dimensional model for the red blood cell, Soft Matter. 6 (2010). https://doi.org/10.1039/C0SM00183J.

[26] S.Z. Hoque, D.V. Anand, B.S.V. Patnaik, The dynamics of a healthy and infected red blood cell in flow through constricted channels: A DPD simulation, Int. J. Numer. Method. Biomed. Eng. 34 (2018) e3105. https://doi.org/10.1002/cnm.3105.

[27] K.I. Tsubota, S. Wada, T. Yamaguchi, Particle method for computer simulation of red blood cell motion in blood flow, Comput. Methods Programs Biomed. 83 (2006) 139–146. https://doi.org/10.1016/j.cmpb.2006.06.005.

[28] H.N. Polwaththe Gallage, S.C. Saha, Y. Gu, Deformation of a single red blood cell in a microvessel, Aust. N. Z. Ind. Appl. Math. J. 54 (2014) 64.

https://doi.org/10.21914/anziamj.v55i0.7828.

[29] J.P. Mills, L. Qie, M. Dao, C.T. Lim, S. Suresh, Nonlinear elastic and viscoelastic deformation of the human red blood cell with optical tweezers, Mech. Chem. Biosyst. 1 (2004) 169–180. https://www.ncbi.nlm.nih.gov/pubmed/16783930.

[30] G. Tomaiuolo, Biomechanical properties of red blood cells in health and disease towards microfluidics, Biomicrofluidics. 8 (2014) 051501. https://doi.org/10.1063/1.4895755.

[31] L.L. Xiao, S. Chen, C.S. Lin, Y. Liu, Simulation of a single red blood cell flowing through a microvessel stenosis using dissipative particle dynamics, Mol. Cell. Biomech. 11 (2014) 67–85. https://www.ncbi.nlm.nih.gov/pubmed/25330624.

[32] D.A. Fedosov, B. Caswell, S. Suresh, G.E. Karniadakis, Quantifying the biophysical characteristics of Plasmodium-falciparum-parasitized red blood cells in microcirculation, Proc. Natl. Acad. Sci. U. S. A. 108 (2011) 35–39. https://doi.org/10.1073/pnas.1009492108.

[33] D.A. Fedosov, B. Caswell, G.E. Karniadakis, A multiscale red blood cell model with accurate mechanics, rheology, and dynamics, Biophys. J. 98 (2010) 2215–2225. https://doi.org/10.1016/j.bpj.2010.02.002.

[34] M. Dao, C.T. Lim, S. Suresh, Mechanics of the human red blood cell deformed by optical tweezers, J. Mech. Phys. Solids. 51 (2003) 2259–2280. https://doi.org/10.1016/j.jmps.2003.09.019.

[35] S. Suresh, J. Spatz, J.P. Mills, A. Micoulet, M. Dao, C.T. Lim, M. Beil, T. Seufferlein, Connections between single-cell biomechanics and human disease states: gastrointestinal cancer and malaria, Acta Biomater. 1 (2005) 15–30.

https://doi.org/10.1016/j.actbio.2004.09.001.

[36] A. Bohiniková, I. Jančigová, I. Cimrák, Modeling Red Blood Cell Viscosity Contrast Using Inner Soft Particle Suspension, Micromachines (Basel). 12 (2021). https://doi.org/10.3390/mi12080974.

[37] H. Zhang, K.-K. Liu, Optical tweezers for single cells, J. R. Soc. Interface. 5 (2008) 671–690. https://doi.org/10.1098/rsif.2008.0052.

[38] S. Chen, N. Phan-Thien, B.C. Khoo, X.J. Fan, Flow around spheres by dissipative particle dynamics, Phys. Fluids . 18 (2006) 103605. https://doi.org/10.1063/1.2360421.

[39] X. Fan, N. Phan-Thien, S. Chen, X. Wu, T. Yong Ng, Simulating flow of DNA suspension using dissipative particle dynamics, Phys. Fluids . 18 (2006) 063102. https://doi.org/10.1063/1.2206595.

[40] Brown Phillip P., Lawler Desmond F., Sphere Drag and Settling Velocity Revisited, J. Environ. Eng. 129 (2003) 222–231. https://doi.org/10.1061/(ASCE)0733-9372(2003)129:3(222).

[41] G. Tomaiuolo, M. Barra, V. Preziosi, A. Cassinese, B. Rotoli, S. Guido, Microfluidics analysis of red blood cell membrane viscoelasticity, Lab Chip. 11 (2011) 449–454. https://doi.org/10.1039/c0lc00348d.

[42] S. Kumari, N. Mehendale, T. Roy, S. Sen, D. Mitra, D. Paul, Measuring RBC deformability and its heterogeneity using a fast microfluidic device, bioRxiv. (2023). https://doi.org/10.1101/2023.07.18.549500.

[43] X. Yang, L.W. Sun, C.F. Du, X.T. Wu, Y.B. Fan, Finite Element Analysis of Osteocytes Mechanosensitivity Under Simulated Microgravity, Microgravity Sci.

Technol. 30 (2018) 469–481. https://doi.org/10.1007/s12217-018-9613-x.

[44] S. Losserand, G. Coupier, T. Podgorski, Migration velocity of red blood cells in microchannels, Microvasc. Res. 124 (2019) 30–36. https://doi.org/10.1016/j.mvr.2019.02.003.